Journal of Industrial and Engineering Chemistry 112 (2022) 389–397

Contents lists available at ScienceDirect

Journal of Industrial and Engineering Chemistry

journal homepage: www.elsevier.com/locate/jiec

# $V_2O_5$ *vs.* $LiFePO_4$: Who is performing better in the 3.4 V class category? A performance evaluation in "Rocking-chair" configuration with graphite anode

Selvarasu Praneetha [a], Yun-Sung Lee [b,*], Vanchiappan Aravindan [a,*]

[a] Department of Chemistry, Indian Institute of Science Education and Research (IISER), Tirupati 517507, India
[b] School of Chemical Engineering, Chonnam National University, Gwang-ju 61186, Republic of Korea

ARTICLE INFO

*Article history:*
Received 15 March 2022
Revised 30 April 2022
Accepted 18 May 2022
Available online 24 May 2022

*Keywords:*
Li-ion battery
$V_2O_5$
$LiFePO_4$
Energy density
Rocking-chair
Pre-lithiation

ABSTRACT

Vanadium pentoxide ($V_2O_5$) brings vast interest in the promising host materials for the intercalation of multivalent ions, owing to its abundance in the earth crust, synthesizing facile methodologies, and offers maximum discharge capacity of >300 mAh $g^{-1}$. However, $V_2O_5$ undergoes different phase transformations upon the intake of beyond 1 mol Li. Here, we report a comparative study of two versatile cathode materials, such as $V_2O_5$ (limiting 1 mol. Li) and $LiFePO_4$. A solvothermal method is adopted to synthesize both two, and three-dimensional crystalline phases of $V_2O_5$ and $LiFePO_4$, respectively. The spherical-shaped $V_2O_5$ exhibits the initial discharge capacity of 136 mAh $g^{-1}$ in the half-cell assembly and renders stable cycle life. Subsequently, $V_2O_5$ is paired with the electrochemically lithiated graphite ($LiC_6$) anode in full-cell assembly ($V_2O_5/LiC_6$) and offers a maximum energy density of ~266.7 Wh $kg^{-1}$ (based on total mass loading). On the other hand, $LiFePO_4$ also exhibits ~136 mAh $g^{-1}$ in the half-cell performance with stable cycle life. The full-cell $LiFePO_4$/C delivers an energy density of ~234.8 Wh $kg^{-1}$. This clearly encourages that $V_2O_5$ is a strong contender for the 3.4 V class Li-ion cells and paves the new avenue for further exploration of advanced battery technologies.


## Introduction

Lithium-ion batteries (LIBs) hold prodigious potential for use in widespread application in portable electronic devices, hybrid electric vehicles (HEVs), and electric vehicles (EVs) due to their high voltage, high energy density, and high power density upon electrochemical lithium intercalation/deintercalation [1]. Growing demands of incipient technologies urgently require high energy density and lightweight with excellent rate performance, better safety at lower cost LIBs [2]. Though the well-established commercially existing cathodes like layered LiCoO2 have limited Li-reversibility, Li1-xCoO2 (x = 0.5, ~137 mAh $g^{-1}$) against the theoretical limitation of ~274 mAh $g^{-1}$ and increasing in price, availability, toxicity will not remain as a preferable cathode in the battery market [3,4].

Recently, $LiNi_{1-x}M_xO_2$ (M = Co, Mn) layered structured Li-rich and Ni-rich oxide can deliver a practical capacity of >250 mAh $g^{-1}$. Conversely, the starting precursors such as Co and Ni are valuable resources that created a major challenge and remained to impede the EVs batteries [5]. Spinel structured $LiMn_2O_4$ is one of the promising cathodes for ample size energy storage for EVs because of higher thermal stability and high rate capability than the cathode mentioned earlier [6]. However, the main problem of spinel cathode is capacity fading upon elevated temperature, which is due to $Mn^{2+/4+}$ dissolution by the disproportion reaction of $2Mn^{3+} \rightarrow Mn^{2+} + Mn^{4+}$. The $Ni^{2+}$ substitution certainly mitigates the Mn dissolution issue, $LiNi_{1.5}Mn_{0.5}O_4$, with the rise in the working potential of 4 to ~4.7 V *vs.* Li owing to the existence of a $Ni^{2+/4+}$ redox couple, but unfortunately falls beyond the thermodynamic stability window of the conventional electrolyte. As a result, the electrolyte is easily getting oxidized at high operating voltage; further investigation needs to be accomplished before its use in EVs [7].

Compared to Co and Mn-oxides containing layered and spinel cathodes, $LiFePO_4$ is considered one of the potential cathodes for high-power large-size next-generation lithium battery applications. Economical, non-toxicity and increased cell safety are the notable salient features. The $LiFePO_4$ has an olivine-type structure

* Corresponding authors.
*E-mail addresses:* leeys@chonnam.ac.kr (Y.-S. Lee), aravind_van@yahoo.com (V. Aravindan).

https://doi.org/10.1016/j.jiec.2022.05.036
1226-086X/

with a theoretical capacity of 170 mAh $g^{-1}$ and a flat voltage profile of 3.45 V *vs.* Li, which makes it a safe cathode with good cycle life upon Li-intercalation/deintercalation [8,9]. However, the $LiFePO_4$ structure has 1D Li-ion transport, and the 3D structural aspect consists of distorted FeO6, LiO6, and PO4 units (Fig. S1). There is no continuous network of edge-sharing FeO6 octahedra to increase the electronic conductivity ($10^{-9}$ to $10^{-10}$ S $cm^{-1}$), which is polaronic in the mixed-valence state, and low lithium ionic diffusivity leads to poor rate capability upon Li-intercalation/deintercalation. This eventually hampers the practical applications to overcome insulator properties and has excellent thermal stability because of strong covalent P-O bonds in the $(PO_4)^{3-}$ anion, but the conductive coating is desperately required for the extraction of Li [10,11]. Stabilizing the $Fe^{2+}$ in the olivine phase requires inert atmospheric sintering, which also increases the processing cost, though the raw material is considered cheap.

Considering issues and challenges in the aforementioned cathode materials, we have endeavored the possibility of using layered $V_2O_5$ as an insertion host. The layered structure consisting of VO5 octahedral units undergoes distortion during the accommodation of Li-ions, along with subsequent multiple reductions of the transition metal from $V^{5+}$ to a mixture of $V^{4+}$ to a mixture of $V^{4+}$ and $V^{3+}$. Generally, Li-intercalation into layered $V_2O_5$ is described as $V_2O_5 + xLi^+ + xe^- \leftrightarrow Li_xV_2O_5$. However, uptake of more than one Li leads to severe structural damage and also results in the absence of a flat ~3.35 V *vs.* Li region as well. Therefore, limiting one mol. Li in the $V_2O_5$ makes this cathode a strong contender for the 3.4 V class category. In contrast to $LiFePO_4$, $V_2O_5$ belongs to the 2D class material by structure and possesses an ionic conductivity in the order of $10^{-3}$ S $cm^{-1}$ at 25 °C [12–15]. Yet, both the materials can be turned into 2D in morphological aspects. Except, the $LiFePO_4$ could not attain the electrochemical performance of $V_2O_5$ without carbon composite. Therefore, in this particular case, $V_2O_5$ exhibits better performance characteristics than $LiFePO_4$ and indicates the attainment of 2D ionic transport pathways of $V_2O_5$ paralleled to the 1D channels in $LiFePO_4$. There are still difficulties in enhancing the cycle life, capacity and stability exist. Simultaneously, there has been research activity going on constructing the $V_2O_5$ electrode structure to reduce the $Li^+$ diffusion distance to improve the overall performance of the cell by adopting other different strategies such as synthesizing 1D nanotubes, rods, and nanowires [16–20]. $V_2O_5$ nanostructures are structurally stable and might improve ionic and electronic transportation through their porous network. On the other hand, hybridizing the carbons with $V_2O_5$ gains electrical conductivity and prevents aggregation [21]. Furthermore, the doping of elements like Ni, Mn, Fe, and Sn into $V_2O_5$ leads to improved electronic conductivity, high structural stability, reduces the charge-transfer resistance, and fastens the kinetics of Faradic reactions [22–25]. Unlike most studies, the intake of more than one-mole Li into a $V_2O_5$ delivers a capacity beyond 300 mAh $g^{-1}$, in particular, beyond two mol. Li forms the irreversible $\omega$-$Li_xV_2O_5$ phase [26]. Recently, our group [28] demonstrated the successful fabrication of $V_2O_5$ with the electrochemically pre-lithiated graphite ($LiC_6$) recovered from spent LIBs by limiting one mol. Li with consistent performance of around 143 mAh $g^{-1}$ at 3.35 V *vs.* Li. Moreover, we have also demonstrated the fabrication of "rocking-chair" type LIBs using $V_2O_5$ as a cathode and spinel $Li_4Ti_5O_{12}$ as an anode, in which both chemical [27] and electrochemical routes [28] were employed for pre-lithiation of the cathode ($Li_xV_2O_5$). Further, we have recently covered the potential use of this fascinating $V_2O_5$ cathode (full-cell assembly) exclusively in the "rocking-chair" and other configurations [29]. The electrochemical charge–discharge profiles of the olivine type $LiFePO_4$ are more appealing. To achieve high-power capability, 2D Li-ion migration into $Li_xV_2O_5$ delivers a flat charge–discharge profile. Finding a suitable anode for fabricating a $V_2O_5$ full-cell assembly is another important issue for practical applications. It is also familiar that the Li-metal anode has severe problems like metal dendrite formation, and decomposing of organic electrolytes during cycling performance leads to safety issues for LIBs. Indeed, graphite anode could accomplish the criteria, but the real challenge is to construct a full-cell assembly with a Li-free cathode like $V_2O_5$. There are few works that reported restricted lithiation into $V_2O_5$; exploring the cathode into the full-cell fabrication is very very rare, particularly with graphite. Theoretically, suppose we pair the graphite with $V_2O_5$; it leads to the working potential of 3.3 V with flat charge–discharge profiles, which is quite remarkable and comparable to the commercially available $LiFePO_4$/C configuration. Importantly, the widely used popular transition metals like Ni, Mn, and Co are not engaged in this LIB. Moreover, there will be 2D Li-ion migration happening between graphite and $V_2O_5$, which leads to a potential outlook to explore high power Li-ion configuration. To date, there is no real comparison available for the fascinating 1D-$LiFePO_4$ and 2D-$V_2O_5$ (limited to 1 mol. Li) cathodes for the fabrication of high-performance LIB power packs with the absence of aforesaid transitional metals.

In this work, we have prepared hierarchical micro/nanostructured spherical shaped crystalline $V_2O_5$ and $LiFePO_4$ rods that have been synthesized by a two-step process that includes a solvothermal method and a post-calcinating treatment. The Li-intercalation/deintercalation of both cathodes was investigated by cyclic voltammograms (CV) and galvanostatic charge–discharge techniques. Full-cells have been constructed with graphite as an anode with two versatile cathodes, $V_2O_5$ and $LiFePO_4$. Prior to the fabrication of the "rocking-chair" type LIBs, detailed Physico-chemical studies were performed along with the half-cell performance and described in detail.

## Experimental section

### *Synthesis of hierarchical $V_2O_5$ microspheres*

$V_2O_5$ microspheres were synthesized via a solvothermal route followed by annealing [38]. In brief, 0.14 mM (0.4 g) of polyvinylpyrrolidone was dissolved in 48 mL of ethylene glycol (EG). Then, vanadium acetylacetonate ($V(acac)_3$ – 18 mM (0.3 g) was mixed with 48 mL EG at 140 °C for 12 h under solvothermal conditions. After the reaction was over, the resultant product was washed with acetone and a water mixture. The obtained $V_2O_5$ powder was calcinated at 500 °C for 2 h in the air atmosphere.

### *Synthesis of $LiFePO_4$ rods*

The $LiFePO_4$ powder was simply synthesized by solvothermal reaction followed by a calcination process [42]. $Fe(O_2CCH_3)_2$ of 0.868 g was dissolved in 20 mL of EG. Then, 0.21 g of $LiOH.H_2O$ and 0.5 g of $H_3PO_4$ were dropwise added to the above solution and kept under stirring for a few minutes. The solution was transferred into a Teflon-lined stainless steel autoclave and heated at 180 °C for 24 h. The intermediate was harvested and washed with acetone and subsequently dried in a vacuum oven. The obtained sample was heated at 700 °C under Ar/ $H_2$ atmosphere to yield the olivine phase carbon-coated $LiFePO_4$.

### *Physical characterization*

The crystal structure was studied by X-ray diffraction (XRD) using Rigaku diffractometer using Cu Kα radiation (λ = 1.5414 A). Morphological features of the synthesized materials were studied using a field emission scanning electron microscope (FE-SEM, S-4700, Hitachi, Japan) and a High-resolution transmission electron

microscope (HR-TEM, HR-TEM, TECNAI, Philips, the Netherlands, 200 keV). STEM nanoprobe mode with High angle annular dark-field imaging (HAADF) detector was employed for the elemental distribution. Raman spectrum of the sample was obtained by Raman spectroscopy (LabRam HR800 UV Raman microscope, Horiba Jobin- Yvon, France).

*Electrode preparation*

Both $V_2O_5$ and $LiFePO_4$ as a cathode in half/full-cell were fabricated along with commercial graphite as anode material. The composite electrode was made by mixing the 70% active material, 20% conductive carbon, and 10% teflonized acetylene black (TAB-2) as a binder. Then, the composite material was made into thin sheets and pressed on a 14 mm diameter stainless steel mesh current collector and was dried for 6 h at 70 °C in a vacuum oven. For the fabrication of the graphite electrode, 80% of active material, 10% conductive carbon, and 10% binder (polyvinylidene fluoride) were mixed with N-methyl pyrrolidone. The slurry was coated onto Cu foil and was dried for over 6 h, and pressed under a hot roll press (Tester Sangyo). An electrode cutter was used to cut the coated Cu foil into a circular disc of 14 mm diameter. Each electrode typically has active material content of ∼2 mg and was dried for 6 h at 75 °C in a vacuum oven. The cells (both half-cells and full-cell) were fabricated in the form of coin cells (CR 2016) in Ar filled glove box. 1 M $LiPF_6$ in EC: DMC (1:1, v/v) electrolyte (Tomiyama, Japan) and Whatman paper (1825–047, GF/F) separator were used for all the cell assemblies. The half-cells were fabricated with $V_2O_5$, $LiFePO_4$, and graphite electrodes with the Li metal counter electrode. The full-cell assembly was done with the $V_2O_5$ or $LiFePO_4$ electrode as the cathode and graphite as an anode. For the case of $V_2O_5$, electrochemically lithiated graphite is used as an anode ($LiC_6$).

*Electrochemical measurements*

A battery tester, BCS 805 (Biologic France), was used to study the electrochemical performance of the assembled coin cells. The diffusion coefficient of Li-ions in both $V_2O_5$ and $LiFePO_4$ half-cell assembly was calculated from the CV profile at different scan rates (0.1–1.0 mV $s^{-1}$). Galvanostatic charge–discharge studies were performed at various current rates in ambient and various environmental conditions. For the case of full-cell assembly with $V_2O_5$, the graphite electrode was electrochemically pre-lithiated ($LiC_6$), in which the graphite electrode was dismantled in the discharged state after two successive cycles. The mass of active material loading in both $V_2O_5$ and $LiFePO_4$ electrodes was adjusted to balance the charge.

## Results & discussion

The polyol process has been commonly adopted for the reduction of metal salts to metal nanoparticles, and particle morphology can be controlled via the addition of surfactant to the mixture. The key parameter in obtaining highly crystalline nanomaterials is the use of a functionalized surfactant as one of the reactants and for controlling the shape of metal oxide nanoparticles [30–34]. The formation of the sphere and rod-shaped morphologies of the active materials are discussed in the forthcoming sections. Fig. 1b shows the X-ray diffraction (XRD) pattern of $V_2O_5$ obtained after calcined at 500 °C in the air from vanadyl glycolate, $VO(CH_2O)_2$. The phase was indexed to the orthorhombic structure with space group *Pmmn* without any impurity peaks. The diffraction peaks of the sample are identified and lattice parameter values are calculated to be $a$ = 11.48, $b$ = 3.56, and $c$ = 4.39 A which is consistent with the standard sample (PDF card no. 01–85-0601). The sharp and high intense peaks at 2θ = 26.19° and 20.31° correspond to the (110) and (001) with an interplanar spacing of 4.36 A and 3.39 A with a layered structure. The average crystallite size of the sample (based on the high-intensity peak) was calculated as ∼76.3 nm using Debye-Scherer's equation. Fig. 1c illustrates the XRD pattern of $LiFePO_4$ calcinated at 700 °C in $Ar/H_2$ atmosphere, and attributed to the olivine phase, showing well-defined sharp reflections, specifying high crystallinity of the sample, which is in good accordance with the standard orthorhombic structure (PDF Card no. 65-0257, space group *Pmna*). The lattice parameters of the olivine phase $LiFePO_4$ are calculated to be $a$ = 10.34, $b$ = 5.29, and $c$ = 4.58 A with a crystallite size of ∼78 nm. Apparently, the crystallite sizes are more or less the same for both orthorhombic phases, and it is worth comparing. The local structure of $V_2O_5$ is determined using Raman spectroscopy, as shown in Fig. 1d**.** The vanadium atom located within the oxygen coordination (V–O bonds) belong to the $D_{2h}$ point group, exhibits polyhedron of four types, and occupies four sites in the [$VO_5$] slab. The band at 405 $cm^{-1}$ corresponds to the V–O1 bond with a shorter and stronger apical band of the rocking mode along the $x$-$z$ plane, and the band at 301 $cm^{-1}$ resembles the oscillation of O1 and O2 atoms combined along $y$- and $z$-directions. The band at 994 $cm^{-1}$ high-frequency mode $v$ (d1) emerges from the stretching vibration of the apical bond. Also, the antiphase stretching of the V–O2 bond appears at 697 $cm^{-1}$ and forms an interchain within the [$VO_5$] slab. The $A_g$ mode located at 526 $cm^{-1}$ shows stretching vibration and displacement of the O2 atom along the $x$-direction. The bending bridge forms between two V atoms as V–O3—V is observed from the band found at 478 $cm^{-1}$. The band appears at 405 and 282 $cm^{-1}$ due to the × and $y$ displacement of the O1 atom, and the band at 301 $cm^{-1}$ is due to the $z$ displacement of the O2 atom. The low-frequency band at 195 $cm^{-1}$ belongs to $A_g$ and $B_{2g}$ modes, whereas the intense band at 142 $cm^{-1}$ belongs to $B_{1g}$ and $B_{3g}$ modes. The shear motion of the ladder and rotation of the ladder is characterized by the $B_{1g}$ and $B_{2g}$ modes. The peak positions are well consistent with previous studies on orthorhombic $V_2O_5$ [35]. As shown in Fig. 1e, $LiFePO_4$ belongs to the point group $D_{2h}^{12}$(*Pnma* space group). The unit cell consists of two cations ($Li^+$ and $Fe^{2+}$) and an anion $PO_4^{3-}$ [36]. The vibration modes above 900 $cm^{-1}$ correspond to the stretching of P–O bonds, and the modes in the 575 and 628 $cm^{-1}$ are ascribed to O–P–O bending internal to the $PO_4^{3-}$ anion. The bands at 1039, 991, and 953 $cm^{-1}$ are attributed to the anti-symmetric stretch ($\nu_3$) and symmetric stretch ($\nu_1$) of the P–O bonds. The bands at 628 $cm^{-1}$ ($A_g$) and modes at 575 and 628 $cm^{-1}$ are attributed to symmetric bend ($\nu_2$) and anti-symmetric ($\nu_4$) of the O–P–O angles, respectively. The mode at 437 $cm^{-1}$ corresponds to the lithium cage modes with translating $Li^+$ and breathing cage surrounding by $O^{2-}$ ions. The bands below 400 $cm^{-1}$ correspond to the translational motion of Fe and coupled translation and vibrational motion of Fe and $PO_4^{3-}$ of $LiFePO_4$. The presence of carbonaceous material is clearly evident from the appearance of characteristic vibration modes at 1335 and 1595 $cm^{-1}$, which are associated with D, and G bands, respectively. Generally, the D band is ascribed to the disordered or defective nature of the carbon originating from hybridized vibrational mode linked with graphene edges and indicates structural defects, whereas the G band originated from the stretching of C–C bonds in graphitic carbon [37]. The high intense D band than the G band is a signature of the amorphous carbon, which is paralleled by calculating the intensity ratio between the D and G bands ($I_D/I_G$). The obtained value of 1.07 clearly represents the poor degree of graphitization. In other words, the carbon layer formed during the synthesis of the olivine phase, $LiFePO_4$, is found to be in amorphous carbon with a concentration of 5.6 wt.%. On the other hand, there are no such carbonaceous traces observed from the Raman spectra

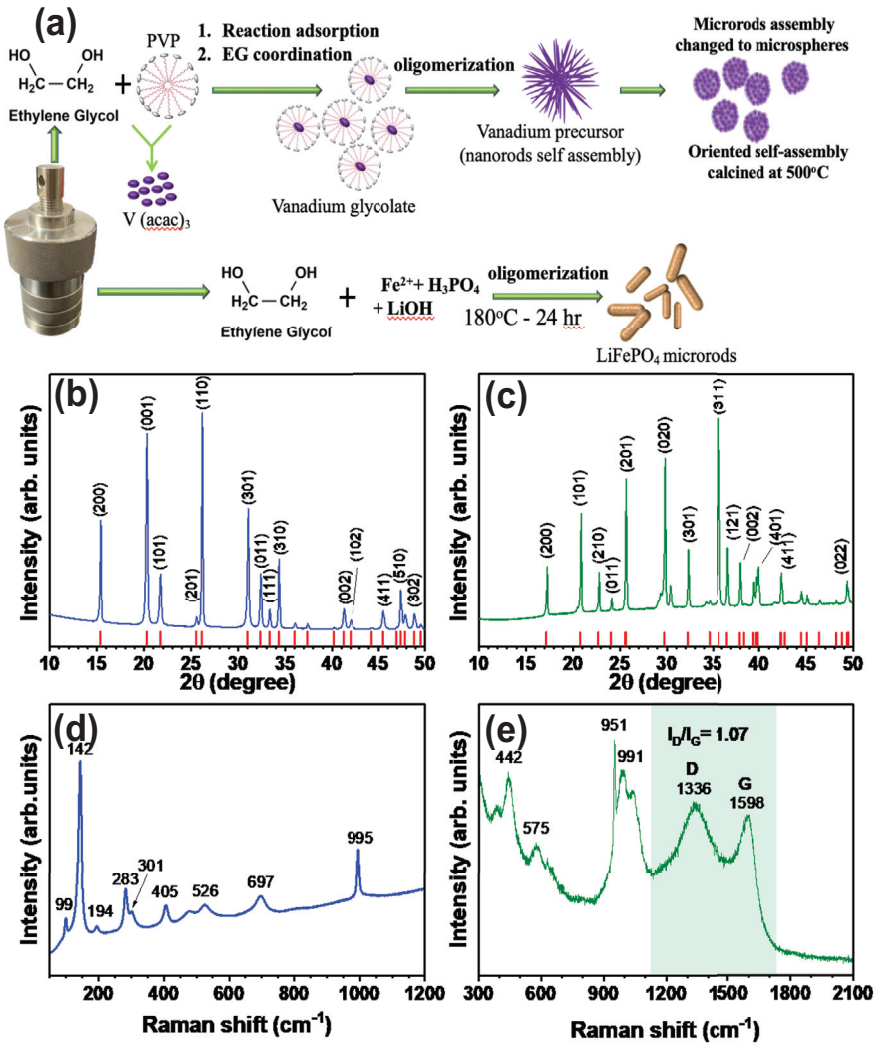


**Fig. 1.** (a) Schematic illustration for the evolution of $V_2O_5$ microsphere and $LiFePO_4$ micro rods; XRD diffraction patterns of solvothermal synthesized, (b) crystalline $V_2O_5$ obtained after calcinated at 500 °C in ambient temperature, (c) $LiFePO_4$ after 700 °C in $Ar/H_2$ atmosphere; Raman spectra for (d) $V_2O_5$, and (e) $LiFePO_4$.

of the $V_2O_5$, though the hydrothermal process is employed for the synthesis.

Field emission scanning electron microscopic (FE-SEM) images showed a disperse of non-agglomerated $V_2O_5$ could be achieved by employing the described solvothermal self-assembly of layered structures (Fig. 2a–c). The layers are formed when $V(acac)_3$ is heated with ethylene glycol at 80 °C form vanadium glycolate followed by an oligomerization reaction [38]. The vanadyl glycolate structure is comprised of 1-D chains that contain edge-sharing VO5 square pyramids (Fig. 1a). The oxygen atoms within the chain derive from a vanadyl group, a chelating (–$OCH_2CH_2O$-) ligand, and one end of two other (–$OCH_2CH_2O$-) ligands present. The addition of polyvinyl pyrrolidone (PVP) into the solution, ascribed to hydrophobic vinyl groups and hydrophilic carbonyl groups, led to the formation of micelles. Thus, the spherical morphology is governed through the oriented aggregation by particle assembly into the microstructure. The carbonyl groups of the PVP chains face outward, and the bidentate [$C_5H_8O_2$] ligand of [$V(acac)_3$] is gradually replaced by EG to form vanadyl glycolate which can be easily adsorbed onto the micelle surface through the abundant hydroxy groups. Specifically, at the initial stage of reaction, the precursors are grown to the layered structure of $V(OH)_2H_2$ through precipitation. With the elapse of time, the number of layers increases and assembled together where the edges are etched by the solvent simultaneously. As time passes, these layer-by-layer structures transform into spherical morphology with a diameter of approximately 5.0 μm, which consists of aggregated primary particles with the indefinite shape of nanoplatelets. Finally, calcination at 500 °C leads to complete oxidation of $V(OH)_2NH_2$ to $V_2O_5$. The formation of rod-like morphology of $LiFePO_4$ is shown in Fig. 2d-f. Here, EG served as both the solvent and reducing agent for the synthesis of $LiFePO_4$ particles. When $H_3PO_4$ was added dropwise into the EG solution of $Fe(O_2CCH_3)_2$, no precipitate was formed in the acidic environment (Fig. 1a). However, a green-black slurry was formed when the $Fe(O_2CCH_3)_2$ with $H_3PO_4$ (Fe acid) mixture was dropwise added into the EG solution of LiOH. This is mainly because Fe-acid solution was added to the high-pH of lithium solution dropwise to form the $Fe^{2+}$–$H_xPO_4^{x-3}$ complexes, and $H_xPO_4^{x-3}$ were converted to amorphous precipitates of $Fe_3(PO_4)_{2(s)}$ and $Li_3PO_{4(s)}$ immediately and appeared as a green-black slurry [39]. Here, The morphology change markedly progresses when the temperature increases to 180 °C, the $LiFePO_4$ phase is formed by dissolution of $Fe_3(PO_4)_2{\cdot}H_2O$ and $Li_3PO_4$. Fig. 2g-l shows the high-resolution transmission electron microscopy (HR-TEM) and elemental mapping of $V_2O_5$ and $LiFePO_4$. The detailed structure of a was analyzed by TEM and their elemental mapping EDX. Fig. 2g-h exhibits a

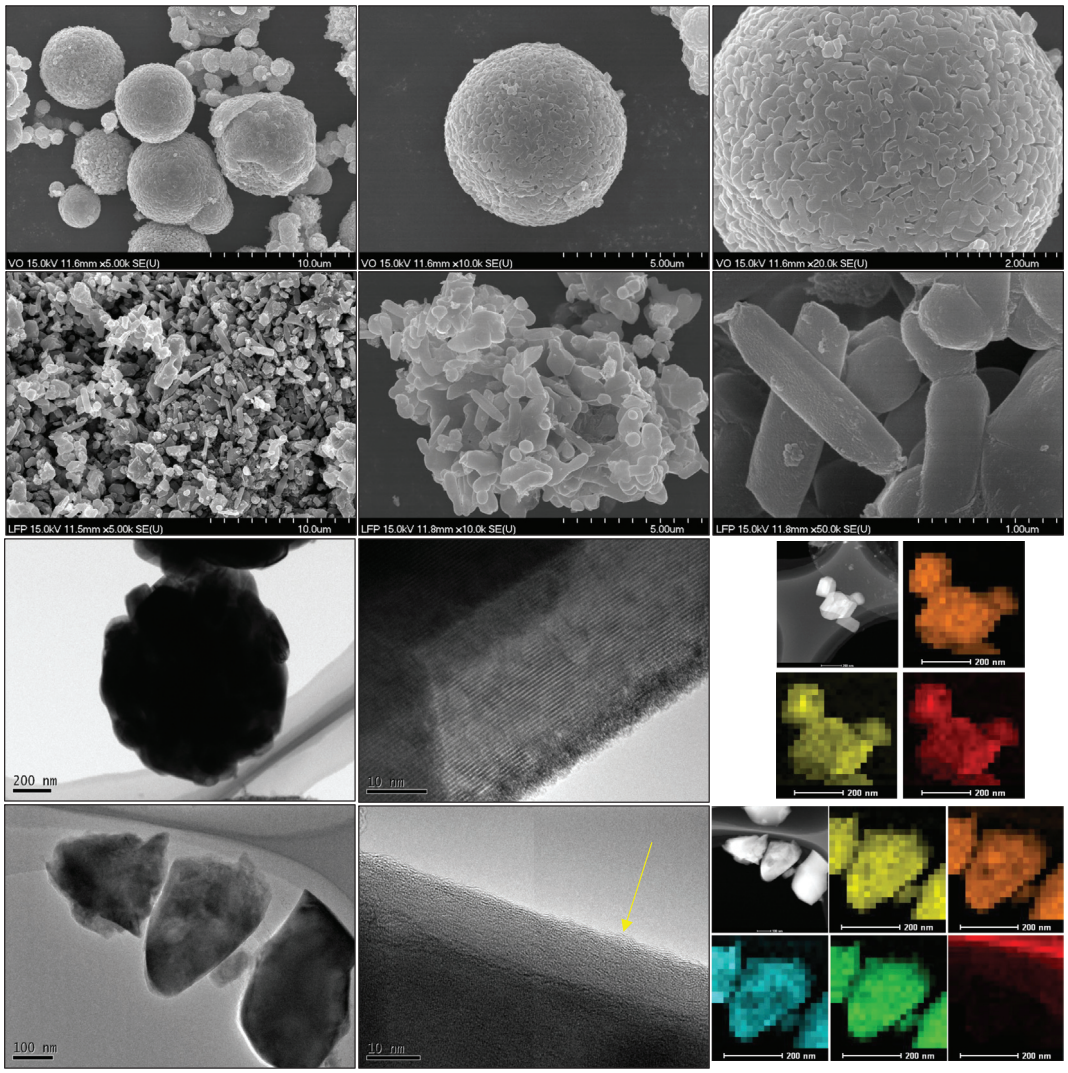


**Fig. 2.** FE-SEM micrographs of (a–c) $V_2O_5$ microspheres and (d–f) $LiFePO_4$ rods like morphology at different magnifications; HR-TEM & EDX images of (g–i) $V_2O_5$, and (j–l) $LiFePO_4$.

highly crystalline hierarchical structure of the $V_2O_5$ microsphere, representing a very dense structure that seems to be composed of staked platelets, consistent with the above SEM results. On the other hand, Fig. 2j-k shows the crystalline $LiFePO_4$ rods uniformly coated with amorphous carbon derived from the residue of EG. In both cases, uniform distribution of the respective elements is noted during the mapping.

A series of comparative electrochemical properties of $V_2O_5$ microspheres and $LiFePO_4$ rods were performed to investigate the Li-insertion properties in half-cell configuration. Fig. S2 shows the CV traces of $V_2O_5$ and $LiFePO_4$ at a scan rate of 0.1 mV $s^{-1}$ from the voltage range of 4.0–2.5 V *vs.* Li. The CV curve shows three cathodic/anodic peaks indicative of phase evolution from $V_2O_5$ to ε-$Li_{0.5}V_2O_5$, δ-$LiV_2O_5$, and γ-$LiV_2O_5$, respectively. The redox peak that appeared at 3.04/3.29 V *vs.* Li disappears in the subsequent cycles, which is evident that the $V_2O_5$ microspheres undergo structural re-arrangement during the first few-cycle, as reported [40]. In the subsequent scans, the peaks at 3.32 and 3.13 V *vs.* Li are only retained and stable, with the small potential separations between the anodic and cathodic peaks indicating good reversibility. With the recent study published by our group [28], limiting the voltage improved the cyclability. In contrast, a very sharp redox profile is observed for the case of olivine phase $LiFePO_4$ with the symmetry of oxidation peak at 3.56 V *vs.* Li and reduction peak at 3.31 V *vs.* Li, which has a less potential difference of 0.25 V, confirming the less polarization than $V_2O_5$. The sharp redox peaks are indicative of a characteristic two-phase reaction. Fig. 3a-b shows the CV curves of $V_2O_5$ microspheres and $LiFePO_4$ rods at scan rates from 0.1 to 1.0 mV $s^{-1}$ within the potential window of 2.5–4 V *vs.* Li. Normally, in the CV traces increase in scan rate is proportional to increased peak current and peak separation. The peak currents $I_p$ (Amperes), during anodic scans at different sweep rates, are used to extract the Li-ion diffusion coefficient $D_{Li}^{+}$ ($cm^2$ $s^{-1}$), applying the Randles-Sevcik equation (Fig. 3c):

$$I_p = 2.69 \times 10^5 A C D^{1/2} n^{3/2} v^{1/2}$$

where $A$ is the electrode area ($cm^2$), C is the shuttle concentration (mol. $cm^{-3}$), $n$ is the number of electrons involved in the redox process ($n$ = 1), and $v$ is the potential scan rate (V $s^{-1}$). According to the slopes of the lines, the Li-diffusion coefficient for $V_2O_5$ is calculated to be 8.57 × $10^{-13}$ (anodic current) and 5.83 × $10^{-13}$ $cm^2$ $s^{-1}$ (cathodic current), and for $LiFePO_4$, significant linear relationship between the cathodic peak current and the square root of scan rates around to be 4.2 × $10^{-9}$ (anodic current) and 2.3 × $10^{-9}$ $cm^2$ $s^{-1}$ (cathodic current). The stability of the CV signal at such a rate reveals

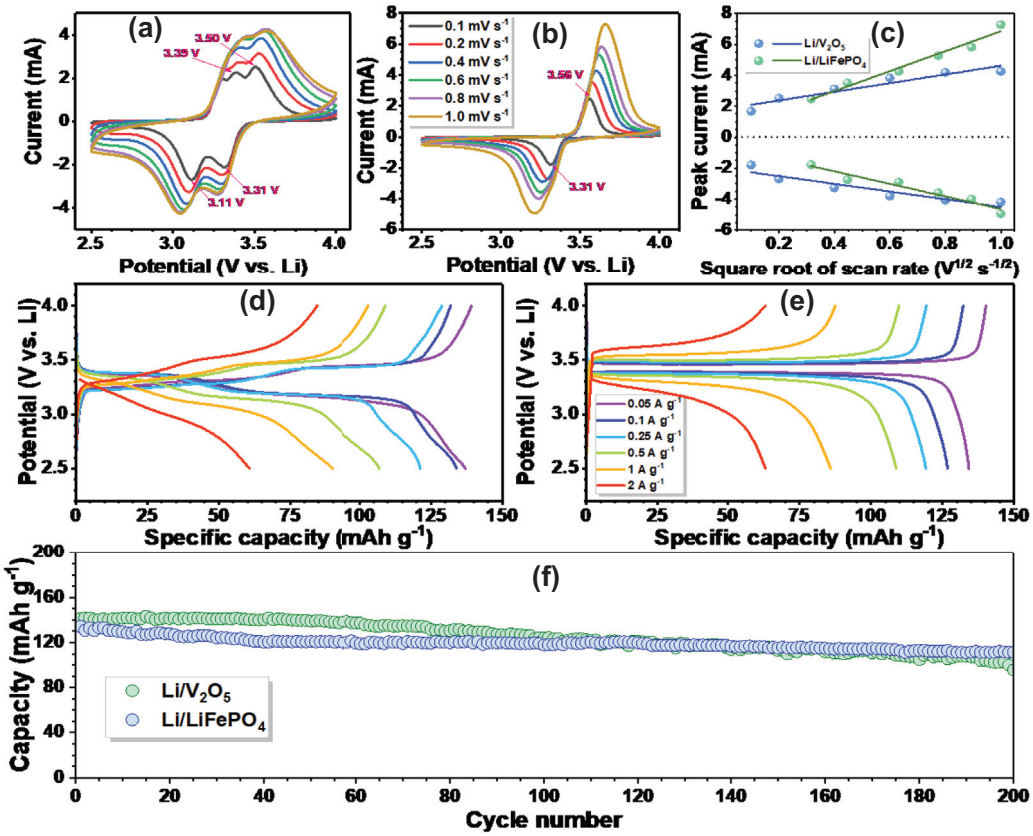


**Fig. 3.** (a,b) Cyclic voltammograms of $Li/V_2O_5$ and $Li/LiFePO_4$ half-cells between 2.5–4 V at various scan rates, (c) Li-ion diffusion calculation for $V_2O_5$ and $LiFePO_4$, (d,e) typical charge -discharge curves of (d) $V_2O_5$, (e) $LiFePO_4$ in half-cell configuration at different current densities ranging from 0.05 to 2 A $g^{-1}$ between 2.5–4 V *vs.* Li, (f) plot of dichsrage capacity *vs.* cycle number $V_2O_5$ and $LiFePO_4$ at current density of 0.5 A $g^{-1}$ upto 200 cycles.

the high power capability of both $V_2O_5$ and $LiFePO_4$ and enables kinetic analysis on a broad sweep rate range.

The galvanostatic charge–discharge profile of both cathodes $V_2O_5$ and $LiFePO_4$ were studied in the potential window of 2.5–4 V *vs.* Li at the current density of 0.05 A $g^{-1}$ in ambient temperature conditions. The test cell delivered a very high initial discharge capacity of ~136 mAh $g^{-1}$ (0.93 mol. of Li), and it is close to the theoretical value of ~147 mAh $g^{-1}$ (1 mol. of Li) for $V_2O_5$ microspheres. The position of plateaus in the discharge curve is in good alignment with the redox peaks observed during the CV analysis (Fig. S2). The large capacity can be attributed in favour of oriented aggregation of particles directed to form microstructure spherical morphology. Fig. 3d & S3 show the galvanostatic charge–discharge profile for the $Li/V_2O_5$ cell at different current densities (0.05, 0.1, 0.5, 1, 1.5, and 2 A $g^{-1}$). As observed in the CV profile, the $V_2O_5$ exhibits a smaller plateau region during both charge and discharge processes which is due to the structural evolution upon the intake of Li. Irrespective of the applied current rate, the $V_2O_5$ exhibits prominent characteristic plateaus, which confirms the structural robustness and integrity. The specific capacity values are calculated based on the mass of active material (~7 mg). At a higher current rate of 2 A $g^{-1}$, the cell could show a capacity value of ~60 mAh $g^{-1}$. There will be low-level ionic penetration that happens at higher current rates. At different current rates, the cell shows stable performance, which indicates the robust nature of the structure with high reversibility. Overall the Li-intercalation process in $V_2O_5$ can be explained with the following equations,

$$V_2O_5 + 0.5Li^+ + 0.5e \leftrightarrow Li_{0.5}V_2O_5 \quad (i)$$

$$Li_{0.5}V_2O_5 + 0.5Li^+ + 0.5e \leftrightarrow LiV_2O_5 \quad (ii)$$

Similar to $V_2O_5$, the half-cell performance of the $LiFePO_4$ rods were conducted under the same testing conditions and given in Fig. 3e & S3. A very prominent and long-plateau is observed at ~3.4 V *vs.* Li, which is consistent with the high intense redox peaks observed during CV studies because of the two-phase reaction (Fig. S2). The $Li/LiFePO_4$ cell delivers the maximum discharge capacity of ~133 mAh $g^{-1}$ (0.78 mol. Li), which is highly comparable to ~136 mAh $g^{-1}$ obtained for $V_2O_5$ under restricted lithiation. Overall, Li-insertion/extraction in $LiFePO_4$ can be represented as follows,

$$LiFePO_4 \leftrightarrow FePO_4 + Li^+ + e^- \quad (iii)$$

Apparently, there is no obvious difference evident for $LiFePO_4$ and $V_2O_5$ in terms of reversible capacity in both high and low current testing conditions. It is worth mentioning that the crystallite size is more or less the same for both cases, though the morphology is different. Another aspect of validating the electrochemical activity is the durability studies, in which both materials are tested for 200 cycles at the current density of 0.5 A $g^{-1}$ and illustrated in Fig. 3f. The half-cell configuration could render the capacities of ~97 and ~110 mAh $g^{-1}$ after 200 cycles for $V_2O_5$ and $LiFePO_4$, which corresponds to the retention of ~71 and ~80% of initial capacity, respectively. Slightly inferior cycling profiles are noted for the case of $V_2O_5$ compared to olivine $LiFePO_4$. This is mainly because of the usage of linear carbonate (DMC)-containing electrolytes since V-based electrodes have poor compatibility with such solutions. However, this issue can be easily eliminated with-

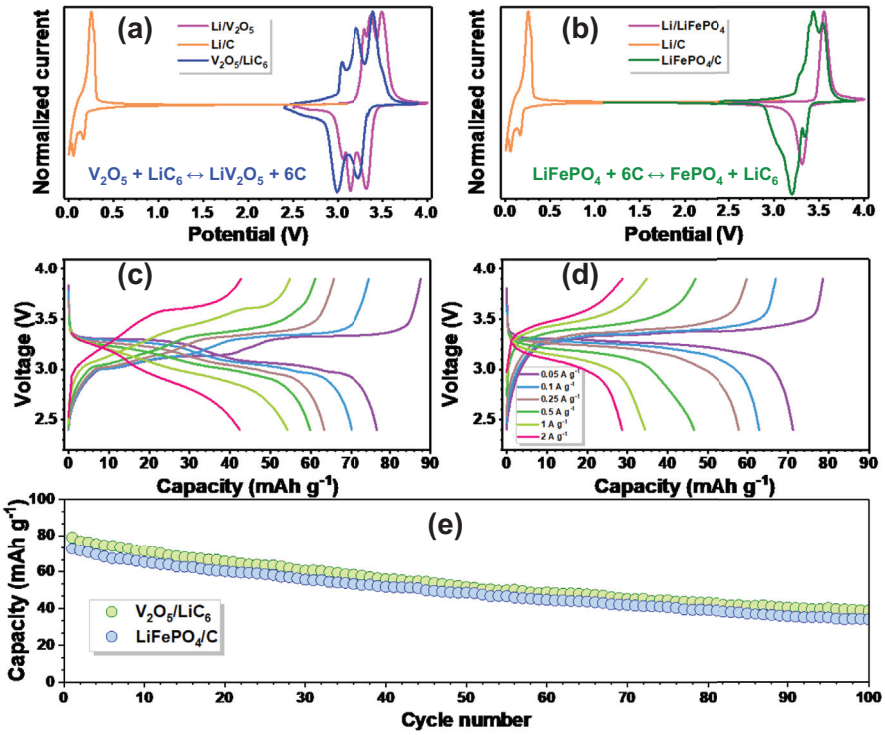


**Fig. 4.** (a, b) Representative CV traces of $V_2O_5$, $LiFePO_4$, and Graphite in half-cell assemblies, $V_2O_5/LiC_6$, and $LiFePO_4$/C full-cells at a scan rate of 0.1 mV $s^{-1}$; Typical charge–discharge curves of, (c) $V_2O_5/LiC_6$, (d) $LiFePO_4$/C at different current densities ranging from 0.05 to 2 A $g^{-1}$ between 2.4–3.9 V, (e) Plot of discharge capacity vs. cycle number for $V_2O_5/LiC_6$ and $LiFePO_4$/C full-cells at a current density of 0.1 A $g^{-1}$ in ambient temperature conditions (25 °C).

out altering the conventional electrolyte by means of adopting carbon coating over $V_2O_5$. This modification certainly hinders the direct exposure to the electrolyte solution and minimizes the inevitable reaction with the electrolyte. An *ex-situ* XRD study was also performed to ensure the structural stability of both cathodes before and after 200 cycles, in which no obvious change in the crystalline nature of the insertion host was noted (Fig. S4). These results clearly suggest that both the cathodes are strong contenders for the fabrication of the 3.4 V class Li-ion cells, in which $LiFePO_4$ is already in the commercial market. It is also worth mentioning that half-cell studies are merely preliminary studies for any kind of electrode material. Therefore, we would like to explore the feasibility of using them in practical application by demonstrating them in full-cell assembly with the graphitic anode.

Pairing the graphite anode with olivine type $LiFePO_4$ for the fabrication of a "rocking-chair" type full-cell assembly is a very straightforward procedure that requires optimizing the mass loading between the electrodes and adjusting the potential window. On the other hand, fabrication requires an additional step of pre-lithiation since there is no free Li available for shuttling between graphite and $V_2O_5$ hosts, besides balancing mass loading and fixation of the potential window. Another interesting fact is that both the graphite and $V_2O_5$ can be efficiently pre-lithiated ($LiC_6$ or $LiV_2O_5$) prior to the fabrication of the full-cell assembly. As mentioned in the introduction, we have already successfully demonstrated the pre-lithiation of both graphite and $V_2O_5$ before pairing in the full-cell assembly. The commercial graphite is subjected to galvanostatic cycling at the current density of 50 mA $g^{-1}$ to adjust the mass loading with either $V_2O_5$ or $LiFePO_4$ cathode in full-cell assembly (Fig. S5). In the present work, the graphite anode has been electrochemically pre-lithiated ($LiC_6$) before coupling it with $V_2O_5$ in full-cell assembly under balanced loading conditions. Accordingly, the graphite electrode undergoes two complete discharge-charge cycles, and the cell has been opened inside the glove box under the discharged state ($LiC_6$). The full-cell assembly (either $V_2O_5/LiC_6$ or $LiFePO_4$/C) comprises more or less the same total active mass loading of ~9 mg. The applied current rate is based on the least mass loading in the full-cell configuration, *i.e.*, graphite, whereas the specific capacity, energy, and power densities were calculated based on the total mass loading of the active materials. Fig. 4a & b depict the CV curves of graphite, $V_2O_5$, and $LiFePO_4$ in half-cell and full-cell assemblies at the scan rate of 0.1 mV $s^{-1}$ in which the current is normalized in the *y*-axis for better comparison. The appearance of a peak at 3.2 and 3.39 V belongs to oxidation, and peaks at 2.99 and 3.23 V represent a reduction of the reversible Li-extraction/insertion within the interplanar space of both $LiC_6$ and $V_2O_5$ electrodes, which is consistent with half-cell studies. The three peaks in the $V_2O_5/LiC_6$ assembly are normally observed ($LiC_6$ and its polarization) in the carbon-based anode configurations. This is quite normal for the case of graphitic carbon-based systems. A similar kind of profile is noted for the case of $LiFePO_4$/C with oxidation (at 3.44 V) and reduction peaks (at 3.35 V) for reversible Li-extraction and insertion. In both full-cell assemblies, the working potential is ~0.1 V lower than the redox potential of the respective cathodes because of the Li-intercalation caused in the graphite anode. Fig. 4c & d illustrate the different current densities (0.05, 0.1, 0.5, 1, 1.5, and 2 A $g^{-1}$) of the galvanostatic charge-discharge cycle of the full-cells between 2.4–3.9 V. The $V_2O_5/LiC_6$ full-cell shows a maximum specific capacity of ~85 mAh $g^{-1}$ at a low current density of 0.1 A $g^{-1}$. At 2.0 A $g^{-1}$ (high current rate), it exhibits a specific capacity of ~41 mAh $g^{-1}$, which is quite remarkable (Fig. S6). Parallelly, the $LiFePO_4$/C cell renders a maximum specific capacity of ~71 and ~29 mAh $g^{-1}$ at a low (0.05 A $g^{-1}$) and high current rates (2 A $g^{-1}$), respectively. Apparently, the $V_2O_5/LiC_6$ cell exhibits marginally better electrochemical activity than the $LiFePO_4$/C assembly. We strongly believe that the presence of two-dimensional pathways for migration of Li-ions and good compatibility with

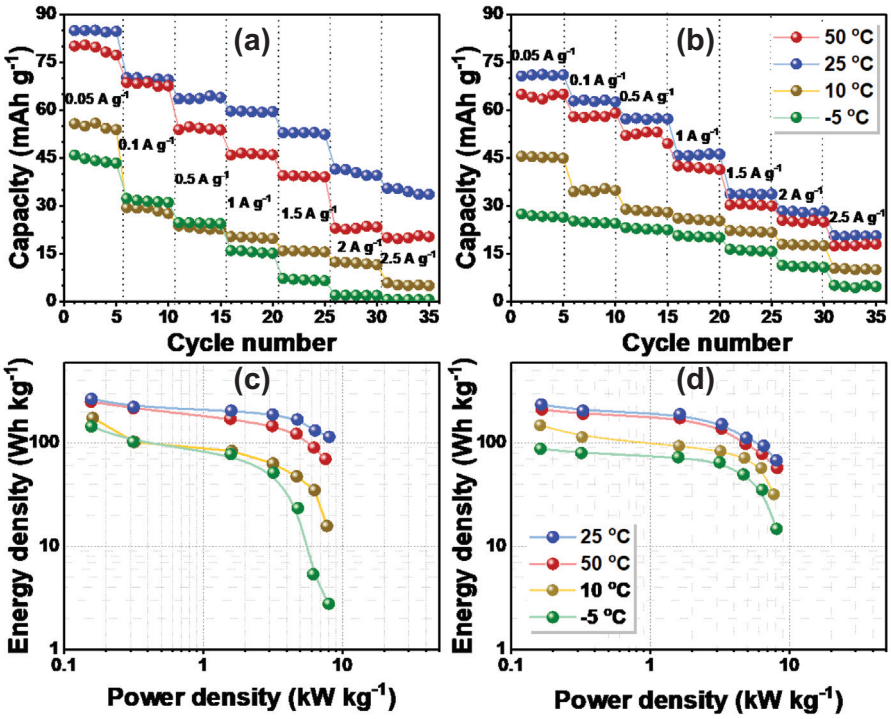


**Fig. 5.** The temperature-dependent rate performance of the assembled full-cell of (a) $V_2O_5$/$LiC_6$ and (b) $LiFePO_4$/C cells between 2.4 to 3.9 V; and the Ragone plot of (c) $V_2O_5$/$LiC_6$ and (d) $LiFePO_4$/C cells. The capacity is calculated based on the total mass loading (anode + cathode) of the active materials.

the lithiated graphite aids in achieving the better electrochemical activity of the $V_2O_5$/$LiC_6$ cell. Cyclability is another aspect of cross-checking the performance of the full-cell, in which both cells are studied at a lower current density of 0.1 A $g^{-1}$ and illustrated in Fig. 4e. The full-cell delivered the discharge capacity of ~79 and ~73 mAh $g^{-1}$ for $V_2O_5$ and $LiFePO_4$-based assemblies, respectively. Also, it retained ~50 and ~47% of initial capacity after 100 cycles. When compared to the respective half-cell performance, both the full-cells experiencing the meager capacity fade upon cycling, but the $V_2O_5$ cathode-based system delivers marginally better performance without any conductive additive, *i.e.,* carbon in $LiFePO_4$. The pre-lithiation process is an additional step required for the fabrication of $V_2O_5$/$LiC_6$ assembly to realize the commercial reality compared to the $LiFePO_4$/C configuration. However, the pre-lithiation process should not hamper the commercial reality since the commercial Li-ion capacitor comprises lithiated graphitic phase as a battery type electrode, and activated carbon serves as a capacitor type component in the same aprotic organic solutions. The pre-lithiation is an exciting topic that not only provides the free Li-ions for the electrochemical reaction but also eliminates the irreversibility observed in the first cycle besides ensuring the half-cell results, which have been detailed in our review [41]. Fig. S7 illustrates the electrochemical impedance spectra (EIS) for both the half-cells and full-cells and gives an idea about the interfacial properties of $V_2O_5$ and $LiFePO_4$. A drastic reduction in the charge-transfer resistance ($R_{ct}$) at the electrode-electrolyte interface is noted for both $V_2O_5$ and $LiFePO_4$; in particular, full-cell assemblies exhibit better compatibility than respective half-cell assemblies.

The full-cell performance at various temperature conditions (50, 25, 10, and −5 °C) has been studied to explore the feasibility of using them in different conditions (Fig. 5). Though the applied current rates are based on the anode mass, the specific capacity, energy, and power density values were calculated by including both the active materials (anode + cathode). Accordingly, the $V_2O_5$/$LiC_6$ cell could deliver a maximum energy density of 266.7, 249.9, 174.3, and 143.8 Wh $kg^{-1}$ at 50, 25, 10, and −5 °C, respectively. However, the $LiFePO_4$/C-based cell displayed an energy density of 210.4, 234.8, 147.1, and 87.6 Wh $kg^{-1}$ for 50, 25, 10, and −5 °C, respectively. Obviously, much better electrochemical performance is noted for the case of $V_2O_5$-based assembly over 1D-$LiFePO_4$ at various temperature conditions. Overall, based on the electrochemical studies, the $V_2O_5$/$LiC_6$ cell is found to be a better candidate than the $LiFePO_4$/C-based system. However, electrochemical properties are not the only factor in determining the scope of the system; other important properties like cell safety, thermal stability, compatibility, etc., have to be studied in more detail. At present, we are focusing the improving the electrochemical performance of the $V_2O_5$ without altering the conventional electrolyte solution, preferably with surface modification.

## Conclusion

Two-dimensional $V_2O_5$ and one-dimensional $LiFePO_4$ were prepared in a facile solvothermal method. Both the cathode materials exhibited similar structural and electrochemical properties. However, multiple electron reactions are possible for the $V_2O_5$ but are limited to one mol. Li-insertion/extraction in this work to ensure stable electrochemical activity. The $V_2O_5$ and $LiFePO_4$ proclaimed their outstanding electrochemical performances in the half-cell system, which logically think us to demonstrate the practical feasibility of fabricating "rocking-chair" type full-cell assembly with a graphite anode. Fabrication of Li-ion cell with $V_2O_5$ cathode and graphite anode requires a pre-lithiation, in which electrochemical pre-lithiation was adopted. Notably, the $V_2O_5$/$LiC_6$ cell could able to attain a maximum energy density of ~266.7 Wh $kg^{-1}$, and the temperature dependence performance studies further

explored the possibility of using them in different atmospheric conditions. As a result, this configuration, $V_2O_5/LiC_6$, is strongly approaching to substitute/emerge the commercially available $LiFePO_4/C$ in the market for various applications and paving a route to construct low-cost energy storage devices.

## Declaration of Competing Interest

The authors declare that they have no known competing financial interests or personal relationships that could have appeared to influence the work reported in this paper.

## Acknowledgements

YSL acknowledges the financial support from the National Research Foundation of Korea (NRF) grant funded by the Korean government (Ministry of Science, ICT & Future Planning) (No. 2019R1A2C1007620). VA acknowledges financial support from the Science and Engineering Research Board (SERB), a statutory body of the Department of Science and Technology, Govt. of India, through Swarnajayanti Fellowship (SB/SJF/2020-21/12).

## Appendix A. Supplementary data

Supplementary data to this article can be found online at https://doi.org/10.1016/j.jiec.2022.05.036.

## Reference

[1] D. Larcher, J.M. Tarascon, Nat. Chem. 7 (1) (2015) 19–29, https://doi.org/10.1038/nchem.2085.
[2] B. Scrosati, J. Hassoun, Y.K. Sun, Energy Environ. Sci. 4 (9) (2011) 3287–3295, https://doi.org/10.1039/c1ee01388b.
[3] Y. Lyu, X. Wu, K. Wang, Z. Feng, T. Cheng, Y. Liu, et al., Adv. Energy Mater. 11 (2) (2021) 2000982, https://doi.org/10.1002/aenm.202000982.
[4] J.B. Goodenough, K.-S. Park, J. Am. Chem. Soc. 135 (4) (2013) 1167–1176, https://doi.org/10.1021/ja3091438.
[5] J. Xu, F. Lin, M.M. Doeff, W. Tong, J. Mater. Chem. A 5 (3) (2017) 874–901, https://doi.org/10.1039/C6TA07991A.
[6] X. Liu, Q. Chen, Y. Li, C. Chen, X. Xing, B. Huang, et al., J. Phys. Chem. C 124 (48) (2020) 26106–26116, https://doi.org/10.1021/acs.jpcc.0c06668.
[7] R. Marom, S.F. Amalraj, N. Leifer, D. Jacob, D. Aurbach, J. Mater. Chem. 21 (27) (2011) 9938–9954, https://doi.org/10.1039/C0JM04225K.
[8] M.S. Whittingham, Chem. Rev. 114 (23) (2014) 11414–11443, https://doi.org/10.1021/cr5003003.
[9] A.K. Padhi, K.S. Nanjundaswamy, J.B. Goodenough, J. Electrochem. Soc. 144 (4) (1997) 1188–1194, https://doi.org/10.1149/1.1837571.
[10] S.-Y. Chung, J.T. Bloking, Y.-M. Chiang, Nat. Mater. 1 (2) (2002) 123–128, https://doi.org/10.1038/nmat732.
[11] R. Malik, D. Burch, M. Bazant, G. Ceder, Nano Lett. 10 (10) (2010) 4123–4127, https://doi.org/10.1021/nl1023595.
[12] A.V. Murugan, B.B. Kale, C.-W. Kwon, G. Campet, K. Vijayamohanan, J. Mater. Chem. 11 (10) (2001) 2470–2475, https://doi.org/10.1039/B100714I.
[13] V. Aravindan, Y.L. Cheah, W.F. Mak, G. Wee, B.V.R. Chowdari, S. Madhavi, Chempluschem 77 (7) (2012) 570–575, https://doi.org/10.1002/cplu.201200023.
[14] X.-T. Gao, X.-D. Zhu, S.-R. Le, D.-J. Yan, C.-Y. Qu, Y.-J. Feng, et al., ChemElectroChem 3 (11) (2016) 1730–1736, https://doi.org/10.1002/celc.201600305.
[15] P. Zhang, L. Zhao, Q. An, Q. Wei, L. Zhou, X. Wei, et al., Small 12 (8) (2016) 1082–1090, https://doi.org/10.1002/smll.201503214.
[16] H. Liu, M.-J. Choe, R.A. Enrique, B. Orvañanos, L. Zhou, T. Liu, et al., J. Phys. Chem. C 121 (22) (2017) 12025–12036, https://doi.org/10.1021/acs.jpcc.7b02819.
[17] G.K.P. Dathar, D. Sheppard, K.J. Stevenson, G. Henkelman, Chem. Mater. 23 (17) (2011) 4032–4037, https://doi.org/10.1021/cm201604g.
[18] P. Gibot, M. Casas-Cabanas, L. Laffont, S. Levasseur, P. Carlach, S. Hamelet, et al., Nat. Mater. 7 (9) (2008) 741–747, https://doi.org/10.1038/nmat2245.
[19] G.A. Horrocks, A. Parija, L.R. De Jesus, L. Wangoh, S. Sallis, Y. Luo, et al., Chem. Mater. 29 (24) (2017) 10386–10397, https://doi.org/10.1021/acs.chemmater.7b03800.
[20] X. Peng, X. Zhang, L. Wang, L. Hu, S.-H.-S. Cheng, C. Huang, et al., Adv. Funct. Mater. 26 (5) (2016) 784–791, https://doi.org/10.1002/adfm.201503859.
[21] X. Wang, Y. Li, S. Wang, F. Zhou, P. Das, C. Sun, et al., Adv. Energy Mater. 10 (22) (2020) 2000081, https://doi.org/10.1002/aenm.202000081.
[22] Y.-Z. Zheng, H. Ding, E. Uchaker, X. Tao, J.-F. Chen, Q. Zhang, et al., J. Mater. Chem. A 3 (5) (2015) 1979–1985, https://doi.org/10.1039/C4TA05500D.
[23] D.M. Yu, S.T. Zhang, D.W. Liu, X.Y. Zhou, S.H. Xie, Q.F. Zhang, et al., J. Mater. Chem. 20 (48) (2010) 10841–10846, https://doi.org/10.1039/C0JM01252A.
[24] X. Yang, J. Leng, D. Wang, Z. Wang, J.-X. Wang, Y. Pu, et al., Chem. Eng. Process. - Process Intensif. 120 (2017) 201–206, https://doi.org/10.1016/j.cep.2017.07.019.
[25] Y. Li, J. Yao, E. Uchaker, M. Zhang, J. Tian, X. Liu, et al., J. Phys. Chem. C 117 (45) (2013) 23507–23514, https://doi.org/10.1021/jp406927m.
[26] C. Delmas, S. Brèthes, M. Ménétrier, J. Power Sources 34 (2) (1991) 113–118, https://doi.org/10.1016/0378-7753(91)85030-Z.
[27] Y.L. Cheah, V. Aravindan, S. Madhavi, J. Electrochem. Soc. 160 (8) (2013) A1016–A1024, https://doi.org/10.1149/2.015308jes.
[28] Y.L. Cheah, V. Aravindan, S. Madhavi, ACS Appl. Mater. Interfaces 5 (8) (2013) 3475–3480, https://doi.org/10.1021/am400666n.
[29] S. Natarajan, S.-J. Kim, V. Aravindan, J. Mater. Chem. A 8 (19) (2020) 9483–9495, https://doi.org/10.1039/D0TA02852E.
[30] C. Liu, X. Wu, T. Klemmer, N. Shukla, X. Yang, D. Weller, et al., J. Phys. Chem. B 108 (20) (2004) 6121–6123, https://doi.org/10.1021/jp0312971.
[31] T. Herricks, J. Chen, Y. Xia, Nano Lett. 4 (12) (2004) 2367–2371, https://doi.org/10.1021/nl048570a.
[32] K.K. Caswell, C.M. Bender, C.J. Murphy, Nano Lett. 3 (5) (2003) 667–669, https://doi.org/10.1021/nl0341178.
[33] J. Chen, T. Herricks, M. Geissler, Y. Xia, J. Am. Chem. Soc. 126 (35) (2004) 10854–10855, https://doi.org/10.1021/ja0468224.
[34] M.-P. Pileni, Nat. Mater. 2 (3) (2003) 145–150, https://doi.org/10.1038/nmat817.
[35] R. Baddour-Hadjean, J.P. Pereira-Ramos, C. Navone, M. Smirnov, Chem. Mater. 20 (5) (2008) 1916–1923, https://doi.org/10.1021/cm702979k.
[36] J. Wu, G.K.P. Dathar, C. Sun, M.G. Theivanayagam, D. Applestone, A.G. Dylla, et al., Nanotechnology 24 (42) (2013) 424009.
[37] A.C. Ferrari, J. Robertson, Phys. Rev. B 61 (20) (2000) 14095–14107, https://doi.org/10.1103/PhysRevB.61.14095.
[38] A.-M. Cao, J.-S. Hu, H.-P. Liang, L.-J. Wan, Angew. Chemie Int. Ed. 44 (28) (2005) 4391–4395, https://doi.org/10.1002/anie.200500946.
[39] S. Yang, X. Zhou, J. Zhang, Z. Liu, J. Mater. Chem. 20 (37) (2010) 8086–8091, https://doi.org/10.1039/c0jm01346c.
[40] J.H. Yao, Z.L. Yin, Z.G. Zou, Y.W. Li, RSC Adv. 7 (51) (2017) 32327–32335, https://doi.org/10.1039/c7ra03885b.
[41] V. Aravindan, Y.-S. Lee, S. Madhavi, Adv. Energy Mater. 7 (17) (2017) 1602607, https://doi.org/10.1002/aenm.201602607.
[42] S. Praneetha, A. Vadivel Murugan, RSC Adv. 3 (47) (2013) 25403–25409, https://doi.org/10.1039/C3RA44133D.